Simulations of Fracture Tests of Uncharged and Hydrogen-Charged Additively Manufactured 304 Stainless Steel Specimens Using Cohesive Zone Modeling

Shin-Jang Sung and Jwo Pan
Mechanical Engineering
University of Michigan
Ann Arbor, MI 48109, USA

Paul S. Korinko, Michael Morgan and Anthony McWillliams
Materials Science and Technology
Savannah River National Laboratory
Aiken, South Carolina, USA

January 2019

Keywords: Modeling, Fracture Toughness Testing, Additive Manufacturing

For publication in Engineering Fracture Mechanics

We Put Science To Work™

Simulations of Fracture Tests of Uncharged and Hydrogen-Charged Additively Manufactured 304 Stainless Steel Specimens Using Cohesive Zone Modeling

Shin-Jang Sung and Jwo Pan[1]
Mechanical Engineering
University of Michigan
Ann Arbor, MI 48109, USA

Paul S. Korinko, Michael Morgan and Anthony McWilliliams
Materials Science and Technology
Savannah River National Laboratory
Aiken, South Carolina, USA

January 2, 2019

Abstract

Fracture tests of uncharged and hydrogen-charged single edge bend specimens of additively manufactured 304 stainless steels are simulated using the cohesive zone modeling (CZM) approach. Two-dimensional plane strain finite element analyses without cohesive elements are conducted to identify the values of cohesive energy. Similar analyses using CZM with the trapezoidal traction-separation laws are then conducted. The best-fit cohesive parameters show the values of cohesive strength for the uncharged specimens are higher than those for the hydrogen-charged ones whereas the value of cohesive energy for the uncharged specimens can be either slightly lower or higher than that for the hydrogen-charged ones.

Keywords: cohesive zone modeling; trapezoidal traction-separation law; fracture test; additive manufacturing; hydrogen effect

---

[1] Corresponding author. Tel.:+1-734-764-9404; fax:+1-734-647-3170
Email address: jwo@umich.edu (Jwo Pan)

Nomenclature

a	crack length
b	remaining ligament length
B	specimen total thickness
B_n	specimen net thickness
CTOD	crack tip opening displacement
CMOD	crack mouth opening displacement
D	diameter of supporting and loading pins
E	Young's modulus
F_i	crack initiation load
F_{max}	maximum load
J_i	J-integral at crack initiation
J_{max}	J-integral at the maximum load
k, n	material constants of tensile true stress-plastic strain curve
L	specimen length
S	span between two supporting pins
L, S, T	building direction, thickness direction and width direction for the AM plate
t	tensile specimen thickness
T	traction
T_0	cohesive strength
X, Y, Z	Cartesian coordinates
w	tensile specimen width

W bend specimen width

Γ_0 cohesive energy

δ separation

δ_0 separation at the end of softening of the traction-separation law

δ_1 separation at the end of the rising part of the traction-separation law

δ_2 separation at the initiation of softening of the traction-separation law

ε_p plastic strain

ν Poisson's ratio

σ true stress

σ_0 yield stress

1. Introduction

The cohesive zone modeling (CZM) approach has been used to model crack extensions in ductile materials [1-10]. With different shapes of the traction-separation laws, the CZM approach can be used for modeling crack extensions in both brittle and ductile materials. Although the CZM approach needs crack paths to be prescribed, this drawback can be mitigated when specimens come with simple (or standard) geometries and boundary conditions, where the crack path is well defined and predictable. Tvergaard and Hutchison [1-3] conducted two-dimensional plane strain finite element analyses of mode I crack extensions of a few plastic zone sizes under small-scale yielding conditions using the CZM approach with the trapezoidal traction-separation law. Their computational results showed the importance of plastic deformation, peak cohesive strength, strain hardening exponent, T-stress, and plastic strain

controlled traction-separation law on the increase of crack growth resistance in ductile metals. Roychowdhury et al. [4] conducted three-dimensional finite element analyses of a large amount of crack growths of one order of magnitude larger than the specimen thickness in C(T) and M(T) specimens using the CZM approach with the exponential traction-separation law. They fitted the load-crack extension curves of C(T) specimens of high constraint and used the calibrated cohesive parameters to predict the load-crack extension curves of the M(T) specimens of low constraint. Scheider and Brocks [5] conducted two-dimensional plane stress finite element analyses of C(T) and M(T) specimens using the CZM approach with a modified trapezoidal traction-separation law [6]. In their following study, Cornec et al. [7] conducted three-dimensional finite element analyses and used the cohesive parameters determined from the notched tensile specimens to simulate the load-displacement curves of the M(T) specimens with a modified trapezoidal traction-separation law.

Chen et al. [8] conducted three-dimensional and two-dimensional plane strain simulations of C(T) specimens using the CZM approach. They showed the stress states near the midsection in the three-dimensional model were different to those in the plane strain model. They also found that the stress triaxiality dramatically varies along the crack front near the side-surfaces and during the initial stage of crack growth. Sigmund and Brocks [9] conducted two-dimensional plane strain simulations of crack extensions in C(T) and M(T) specimens using the CZM approach with the exponential traction-separation law. The cohesive parameters were estimated from using the Gurson model with consideration of stress triaxiality to fit the J-R curves. Recently, Woelke et al. [10] conducted finite element analyses of the crack growth of many times of the thickness of edge-cracked specimens using shell elements to fit the load-displacement curves with a rigid trapezoidal traction-separation law. For the ductile plate in

4

their study, the crack needs to advance about seven times of the plate thickness to reach a larger steady-state cohesive energy from a smaller initial cohesive energy.

In this investigation, small rectangular single edge bend (SE(B)) specimens were cut in different orientations from an additively manufactured (AM) 304 stainless steel plate built by LENS (Laser Engineered Net Shaping). The AM steel plate is anisotropic with respect to the building direction and the laser movement direction [11] and it is expected that the fracture behavior depends on the orientation. Also, the material properties are different with respect to the distance to the base plate where the AM plate was built [12]. In this paper, we only examine the fracture properties of the SE(B) specimens of two orientations as the first exploratory effort to apply the CZM approach to model the fracture behavior of AM materials with anisotropic mechanical and fracture properties. In contrast to the previous research work, the rectangular SE(B) specimens with side-grooves used in this investigation are small and under fully yielded conditions at crack initiation and during crack growth. The active plastic zone sizes decrease near the crack tips in the specimens during crack growths. Also, the crack extensions in the specimens are nearly to the halves of the ligament sizes in the range of a few millimeters. The effects of the plastic flow on the crack growth behavior can be quite different from those under small scale yielding conditions.

In contrast to the previous works, the load-displacement-crack extension data and the experimental J-R curves are available from the fracture tests. Therefore, the simulation results can be compared to the experimental load-displacement, load-crack extension, crack extension-displacement, and J-crack extension curves to select the fitting cohesive parameters for the cohesive zone modeling approach. In this investigation, hydrogen embrittlement effects on the AM stainless steels are only explored from the cohesive parameters identified in the simulation

results to fit the experimental load-displacement, load-crack extension, crack extension-displacement, and J-crack extension curves. Detailed modeling of hydrogen embrittlement and cohesive zone modeling for conventional steels can be found in two review papers [13, 14]. The cohesive zone modeling approach coupled with hydrogen diffusion as discussed in [14] is not considered in this investigation and is out of the scope of this paper.

In this paper, the experimental results of the SE(B) specimens are first presented to show the J-R curves for uncharged and hydrogen-charged SE(B) specimens of AM stainless steels and the effects of the hydrogen on the J-R curves. Then, two-dimensional plane strain finite element analyses of the SE(B) specimens of different orientations without cohesive elements to estimate the values of the J-integral at crack initiation or the cohesive energy are presented. Next, two-dimensional plane strain finite element analyses of the SE(B) specimens of different orientations with cohesive elements to fit the load-displacement-crack extension data and the J-R curves to identify the values of the other fitting cohesive parameters are presented. Finally, some conclusions are made.

2. Experimental Results of Fracture Tests

Fracture tests were conducted using uncharged and hydrogen-charged single edge bend (SE(B)) specimens of additively manufactured (AM) 304 stainless steels. Details of the specimens and the experiments will be presented in a future publication. In this investigation, these SE(B) specimens were cut in different orientations from a fully dense rectangular plate built by LENS (Laser Engineered Net Shaping), a type of directed energy deposition (DED) technology. Half of the SE(B) specimens before tests were charged with hydrogen to the hydrogen concentration of 2,700 appm. Figure 1(a) shows an AM plate, the orientations of the

AM plate, and SE(B) specimens of different orientations. In the figure, L is the stacking direction (building direction), S is the thickness direction and T is the width direction. The interfaces between layers are represented by gray lines. The orientations of interest in this investigation are only the LS and TS orientations. For example, the notation LS in Figure 1(a) indicates that the length and width of the fracture specimen are along the L and S directions, respectively. Figure 1(b) shows a schematic of an LS SE(B) specimen. Figure 1(c) shows a schematic of a TS SE(B) specimen. As shown in Figures 1(b) and (c), schematics of LS and TS tensile specimens are also plotted as inserts. As shown in the figures, the tensile properties for the materials in the direction perpendicular to the crack planes are determined and later used as the input material properties to simulate the fracture tests of the SE(B) specimens. Figure 2 shows a schematic of an SE(B) specimen with one loading pin and two supporting pins. The SE(B) specimens were side-grooved with slightly different side-grooving depths. The specimen length L and the span S between the two supporting pins are 49.734 mm and 43.18 mm, respectively, for all specimens. The dimensions of the crack length a, the thickness B, the net thickness B_n, the width W, and the remaining ligament length b are listed in Table 1 for the uncharged and hydrogen-charged SE(B) specimens in the LS and TS orientations. The clip gauge was attached to the two notch tips on the lower surfaces of SE(B) specimens as shown in Figure 2. The initial crack mouth opening is 2.54 mm.

Figure 3 show the load-displacement, load-crack extension and crack extension-displacement curves for the uncharged and hydrogen-charged LS SE(B) specimens. Figure 4 show the load-displacement, load-crack extension and crack extension-displacement curves for the uncharged and hydrogen-charged TS SE(B) specimens. The displacement of interest in this investigation is the crack mouth opening displacement (CMOD) measured by the clip gauge.

Figures 5 and 6 show the J-R curves for the uncharged and hydrogen-charged LS and TS SE(B) specimens, respectively, obtained from the ASTM Standard E1820 [15]. In Figures 5 and 6, the lower J-R curves for the hydrogen-charged LS and TS SE(B) specimens indicate harmful effects of hydrogen on the ductility of this AM 304 stainless steel. As shown in Figures 5 and 6, $J_{0.2}$, $J_{\max}$ and J_i are marked in the figures, and the lines with the slope of $2\sigma_0$ from the crack extension of 0.2 mm are also shown. As shown in Figure 5, the $2\sigma_0$ line does not intersect the J-R curve with the crack extension of 2.4 mm for the uncharged LS SE(B) specimen. Therefore, only $J_{0.2}$ for the hydrogen-charged specimen can be determined. $J_{\max}$ is the J-integral at the maximum load.

In Wu et al. [16], the values of the cohesive energy were selected as those of $J_{\max}$ corresponding to the maximum loads for the arc-shaped specimens of uncharged and hydrogen-charged conventionally forged (CF) steels in their simulations of the crack extensions in the specimens. The computational results in Wu et al. [16] indicated that the load-displacement and crack extension-displacement curves from the simulations are compared reasonably well with the experimental data. However, the selection of the cohesive energy corresponding to $J_{\max}$ will not give the load-crack extension and J-R curves in agreement with the experimental results. Therefore, an alternate approach of selecting the cohesive energy as the J-integral at crack initiation, J_i, for a given specimen will be developed. The definition of crack initiation in this study will be explained in the next section. Table 2 lists the values of the crack initiation load F_i, the maximum load $F_{\max}$, the J-integral at crack initiation, J_i, the J-integral at the maximum load, $J_{\max}$, and the crack extensions corresponding to J_i and $J_{\max}$ for the uncharged and hydrogen-charged LS and TS SE(B) specimens. The crack extensions corresponding to J_i and

8

J_{max} will be discussed in Section 4. Finally, it should be mentioned that the J-R curves for the uncharged and hydrogen-charged LS SE(B) specimens are higher than those of the uncharged and hydrogen-charged TS SE(B) specimens, respectively. The higher J-R curves for the LS SE(B) specimens are consistent with the higher failure strains of the LS tensile specimens as shown in Figure A4 in Appendix A. The J-R curves for the hydrogen-charged LS and TS SE(B) specimens are lower than those of the uncharged LS and TS SE(B) specimens, respectively. The lower J-R curves for the hydrogen-charged LS and TS SE(B) specimens show the effects of hydrogen embrittlement on the AM stainless steels.

3. Two-Dimensional Finite Element Analyses of Fracture Tests without CZM

3.1 Two-Dimensional Finite Element Models of Half Specimens

Two-dimensional finite element analyses without CZM for the uncharged and hydrogen-charged LS and TS SE(B) specimens are firstly conducted to obtain the estimates of the cohesive energy corresponding to crack initiation in these specimens. Due to the symmetry conditions, only the right half of the uncharged LS SE(B) specimen is modeled as shown in Figure 7. The Cartesian $X-Y$ coordinate system is also shown in Figure 7. The geometric dimensions for the uncharged and hydrogen-charged LS and TS SE(B) specimens are listed in Table 1. The detailed design of the notches for mounting the clip gauge for measuring the CMOD is not modeled since the region near the mounting notches hardly deforms. However, computational displacements are still collected from the locations of two notch tips shown in Figure 2 for the CMOD. The location to take the initial CMOD is marked as a red dot in Figure 7. The computational initial CMOD is 2.6 mm, slightly higher than the experimental value of 2.54 mm. For simplification, the loading pin and the supporting pin with the same radius of 3.175 mm are modeled as

9

analytical rigid bodies. The contact interfaces between the pins and SE(B) specimens are modeled with no-penetration in the normal direction and frictionless in the tangential direction. The X-symmetry boundary condition is applied along the ligament, marked in blue in Figure 7. The supporting pin contacting the lower surface of the specimen is fixed, and a downward displacement is applied to the loading pin on the top surface of the specimen.

Three element sizes of 0.1 mm by 0.1 mm, 0.2 mm by 0.2 mm and 0.4 mm by 0.4 mm are used in the finite element model. The smallest elements of 0.1 mm by 0.1 mm are located near the crack and the ligament, and near the contact surfaces. Plane strain linear elements with full integration (CPE4) are exclusively used. Similar finite element models for the hydrogen-charged LS specimen, and the uncharged and hydrogen-charged TS specimens are also developed. The finite element models are similar to that shown in Figure 7 and will not be shown here. Two material definitions for the uncharged AM 304 stainless steel in the LS orientation were obtained from two tensile test results, as discussed in Appendix A. The values of the Young's moduli are 190 GPa and 166 GPa, and the Poisson's ratio is 0.3. The input true stress-plastic strain curves are shown in Figure A3(a). The same two material definitions are also used for the hydrogen-charged AM 304 stainless steels in the LS orientation due to lack of the corresponding tensile test results. Similarly, the Young's modulus, the Poisson's ratio and input true stress-plastic strain curves for the uncharged TS specimen presented in Appendix A are used for the uncharged and hydrogen-charged TS specimens. It should be mentioned that the true stress-plastic strain curves for the TS tensile specimens are higher than those of the LS tensile specimens. The commercial finite element program ABAQUS was employed to perform the analyses of the LS and TS SE(B) specimens with consideration of geometric nonlinearity.

3.2 Computational Results

Figures 8(a) and (b) show the computational and experimental load-displacement curves for the uncharged and hydrogen-charged LS SE(B) specimens, respectively. Figures 9(a) and (b) show the computational and experimental load-displacement curves for the uncharged and hydrogen-charged TS SE(B) specimens, respectively. In these figures, the initial parts of the computational load-displacement curves agree well with the experimental data. In addition, the computational results with the two material definitions obtained from two tensile tests for each orientation are very similar. Therefore, only the material definitions for the tensile specimens #28 and #16 for the LS and TS orientations, respectively, were adopted for the following discussions and simulations. As shown in Figures 8(b) and 9(b), the initial parts of the computational and experimental load-displacement curves for the hydrogen-charged SE(B) specimen are also in agreement. This suggests that the use of the tensile stress-strain curves for the uncharged specimen to simulate the fracture behavior of the hydrogen-charged specimen can be reasonable.

In this investigation, the crack initiation is defined when the computational load-displacement curves start to deviate from the experimental ones. As shown in Figures 8(a) and (b), the values of the crack initiation load F_i for the uncharged and hydrogen-charged LS SE(B) specimens are selected to be 2,050 N and 2,750 N, respectively. For the uncharged and hydrogen-charged TS SE(B) specimens, the values of the crack initiation load F_i are selected to be 2,200 N and 2,400 N, respectively, as shown in Figures 9(a) and (b). The plastic zones at crack initiation for the uncharged and hydrogen-charged LS and TS SE(B) specimens are plotted in red in Figures 10(a) and (b) and Figures 11(a) and (b), respectively. As shown in the figures, the plastic zones at crack initiation are fully developed ahead of the crack tips across the

remaining ligaments. However, the bulks of the SE(B) specimens are still in elastic states. Note that the tensile specimens were cut from the elastic portions of the SE(B) specimens. The values of the crack initiation load F_i and the J-integral at the crack initiation load, J_i, for the uncharged and hydrogen-charged LS and TS SE(B) specimens are listed in Table 2. In the next section, the values of J_i will be used as the values of the cohesive energy Γ_0 for the given specimens. It should be mentioned that the finite element size of 0.1 mm selected in this investigation is about one eighth of the plastic zone sizes for both LS and TS SE(B) specimens at crack initiation. The selection of the finite element size relative to the plastic zone size is comparable to that in Tvergaard and Hutchison [1-3]. When a smaller finite element size is selected, our finite element analyses encounter numerical difficulties.

4. Two-Dimensional Finite Element Analyses of Fracture Tests with CZM

4.1 Cohesive Zone Modeling

The cohesive zone modeling (CZM) approach is adopted to model the crack extensions in the uncharged and hydrogen-charged LS and TS SE(B) specimens in this investigation. Cohesive elements with zero thickness are inserted along the prescribed crack path between the regular continuum elements to model the interfacial mechanical behavior in the normal direction. Various traction-separation laws and frameworks of cohesive elements were developed for different applications. In this investigation, the framework of the two-dimensional cohesive elements in [17] was adopted with the trapezoidal traction-separation law presented in [6]. The choices are suitable for modeling ductile fracture with consideration of large deformation. Figure 12 shows a schematic of the normalized trapezoidal traction-separation law. The traction-separation law consists of three polynomials as

$$T = \begin{cases} T_0 \left[2\left(\dfrac{\delta}{\delta_1}\right) - \left(\dfrac{\delta}{\delta_1}\right)^2 \right] & 0 \le \delta < \delta_1 \\[2mm] T_0 & \delta_1 \le \delta < \delta_2 \\[2mm] T_0 \left[2\left(\dfrac{\delta - \delta_2}{\delta_0 - \delta_2}\right)^3 - 3\left(\dfrac{\delta - \delta_2}{\delta_0 - \delta_2}\right)^2 + 1 \right] & \delta_2 \le \delta < \delta_0 \end{cases} \qquad (1)$$

where T is the traction and T_0 is the cohesive strength. The separation is represented by δ and

the final separation is represented by δ_0 when the traction becomes zero. The δ_1 is the

separation at the end of the initial part of the traction-separation law. The δ_2 is the separation at

the onset of softening.

The cohesive energy Γ_0 is defined as the area under the traction-separation curve. The

unit of the cohesive energy Γ_0 is the same as that of the J-integral. It should be noted that δ_1

should be small enough to prevent inducing too much artificial compliance but large enough to

assure computational stability. Therefore, there are only three independent cohesive parameters

in the trapezoidal traction-separation law. In this investigation, these three independent

parameters are chosen as the cohesive energy Γ_0, the cohesive strength T_0, and the softening

ratio δ_2/δ_0. The softening ratio δ_2/δ_0 can be treated as a shape factor. The shape of the

traction-separation law with a large δ_2/δ_0 is close to a rectangle, and with a small δ_2/δ_0 is close

to a triangle. The ratio δ_1/δ_0 is selected to be small as 0.005 for all simulations. The small ratio

δ_1/δ_0 gives a very stiff initial linear response and a very small cohesive energy for the initial

linear part. Since the remaining ligament of an SE(B) specimen is mainly subjected to bending,

the upper part of the ligament is under compression. For $\delta < 0$, an elastic response with a large

stiffness (500 times of the initial tensile stiffness) is assigned to prevent significant overlap of

two adjacent continuum elements. The cohesive energy Γ_0 is chosen as the value of J_i from

the experiment for each specimen. The cohesive strength T_0 and the softening ratio δ_2/δ_0 are

chosen as two fitting parameters to fit the load-displacement, load-crack extension, crack

extension-displacement and J-crack extension data for each specimen. Since the softening ratio

δ_2/δ_0 has a minor influence on the simulation results as discussed later in this paper, the main

fitting parameter is the cohesive strength T_0.

4.2 Two-Dimensional Finite Element Models of Full Specimens

Two-dimensional finite element models with cohesive elements for the uncharged and

hydrogen-charged LS and TS SE(B) specimens are developed to fit the experimental data of the

fracture tests. The prescribed crack paths are straight and parallel to the initial cracks. The full

specimens are modeled by creating horizontally flipped meshes from the ones used in the

previous section. The two corresponding meshes are then joined with the cohesive elements

placed along the prescribed crack paths for the SE(B) specimens. Figure 13 shows only the

finite element model for the uncharged LS SE(B) specimen. The Cartesian $X - Y$ coordinate

system is also shown in the figure. Only the material definition for the tensile specimen #28 is

considered as the input for the uncharged and hydrogen-charged LS SE(B) specimens. The

contact definitions are the same as those for the half specimens. For the boundary conditions, the

supporting pins are fixed, and a downward displacement is applied to the loading pin. In order to

avoid excess overlap in the severely compressive region and constrain the rigid body motion in

the X direction, the X-symmetry boundary condition is applied to a small portion of the crack

paths (about 0.5 mm) near the upper surface of the specimen, marked in yellow in Figure 13.

The finite element models for the other three cases are similar to the one in Figure 13 and will

not be shown here. The commercial finite element program ABAQUS was employed to perform the analyses with consideration of geometric nonlinearity.

4.3 Computational Results

The sets of the cohesive parameters for the uncharged and hydrogen-charged LS and TS SE(B) specimens are determined and listed in Tables 3 and 4, respectively. It is noted that in this investigation, the softening ratio δ_2/δ_0 of 0.3 is selected for all SE(B) specimens except for the uncharged LS SE(B) specimens with the softening ratio δ_2/δ_0 of 0.22 due to the numerical difficulty when a larger softening ratio δ_2/δ_0 is selected. In general, the softening ratio δ_2/δ_0 has a minor influence on the simulation results of the load-displacement, load-crack extension, and crack extension-displacement curves. Therefore, the cohesive strength T_0 is the only main fitting parameter for identification in this investigation. Figures 14 and 15 show the traction-separation laws and the normalized ones for the uncharged and hydrogen-charged LS and TS specimens, respectively. As shown in Figure 14(a) and listed in Table 3, the cohesive strength and energy for the uncharged LS SE(B) specimen are both higher than those for the hydrogen-charged LS SE(B) specimen. However, as shown in Figure 15(a) and listed in Table 4, the cohesive strength for the uncharged TS SE(B) specimen is higher than that for the hydrogen-charged TS SE(B) specimen while the cohesive energy for the uncharged TS SE(B) specimen is lower than that for the hydrogen-charged TS SE(B) specimen. The lower cohesive energy for the uncharged TS SE(B) specimen will be discussed later.

Figures 16 to 19(a) to (c) show the computational and experimental load-displacement, load-crack extension, and crack extension-displacement curves for the uncharged and hydrogen-charged LS and TS SE(B) specimens, respectively. As shown in Figures 16(a) to 19(a), the

computational load-displacement curves agree well with the experimental results. However, Figures 16(b) and (c) to 19(b) and (c) show that the use of cohesive zone modeling (CZM) in this study cannot fully capture the initial parts of the load-crack extension and the crack extension-displacement curves. This is unavoidable due to the usage of constant cohesive parameters along the crack path if the general trends of curves are of interest. Figures 16(d) to 19(d) show the computational and experimental J-R curves for the uncharged and hydrogen-charged LS and TS SE(B) specimens based on the ASTM Standard E1820 [15]. Again, the initial parts of the J-R curves cannot be fully captured using the CZM approach with the constant cohesive parameters along the crack path. However, the computational J-R curves for the uncharged and hydrogen-charged LS and TS SE(B) specimens have the same general trends as those of the experimental data. In order to capture the responses of the early stages from the initiation of crack growth to the steady-state growth, a rising cohesive energy along the crack path may be used [10]. In this exploratory study, CZM has been only used to qualitatively explain the effects of hydrogen through two cohesive parameters: the cohesive strength T_0 and the cohesive energy Γ_0.

For the load-displacement and load-crack extension curves shown in Figures 17(a) and (b) to 19(a) and (b), there are oscillations of the loads as the displacement and crack extension increase. The oscillations are larger in Figures 18(a) and (b). The reasons are that the values of the cohesive strength for these cases are selected to be relatively high to fit the load-displacement curves with the relatively low given values of the cohesive energy. Therefore, the load decreases slightly as the traction of the cohesive element ahead of the crack tip decreases. As listed in Table 2, the crack extensions corresponding to crack initiation identified from the finite element analyses without cohesive elements are small and less than 0.15 mm. The crack extension for the uncharged TS SE(B) specimen is very small at 0.04 mm so the corresponding J-integral at

this crack extension is also very small at 40 kJ/m^2. Consequently, the cohesive strength must be selected to be very high at $5.48\,\sigma_0$. A smaller crack initiation load and crack extension can also be selected. Then an even higher cohesive strength needs to be selected to fit the load-displacement curve. With a very high cohesive strength, numerical instability occurs. For the uncharged TS SE(B) specimen, the cohesive energy Γ_0 is smaller than that for the hydrogen-charged TS SE(B) specimen. With the lower cohesive energy Γ_0 for the uncharged TS SE(B) specimen, the computational J-R curve is still higher than that for the hydrogen-charged TS SE(B) specimen from the simulations. In general, when a larger value of the cohesive energy is selected, a lower cohesive strength can be selected to fit the load-displacement curve. However, the initial rising part of the load-crack extension curve will become smaller so the displacement at the maximum load will be at a smaller crack extension. When the cohesive energy is selected to be large and corresponding to the J-integral at the maximum load, the rising part of the load-crack extension curve disappears, as presented in Wu et al. [16] for CF stainless steels. In Table 2, the crack extensions and the J-integrals at the maximum loads are also listed. As listed in the table, the crack extensions corresponding to the J-integrals at the maximum loads are all large and larger than 0.5 mm.

Finally, the selected lower cohesive strengths for the hydrogen-charged specimens when compared to those of the uncharged specimens appear to be in agreement with the general trends discussed on hydrogen embrittlement in the literature [13, 14]. However, the selected lower cohesive energy for the uncharged TS SE(B) specimen when compared to that for the hydrogen-charged one appears to be different from the trend discussed on hydrogen embrittlement in the literature [13, 14]. It should be mentioned again that the lower cohesive energy of the uncharged TS SE(B) specimen is chosen from the lower J_i from fitting the load-displacement curve of the

uncharged TS SE(B) specimen. However, even with the lower J_i for the uncharged TS SE(B) specimen, the major fitting cohesive strength T_0 must be chosen to be a higher value than that of the hydrogen-charged TS SE(B) specimen in order to fit the experimental load-displacement-crack extension data and J-crack extension curve of the uncharged TS SE(B) specimen.   The higher value of the cohesive strength gives much larger J-integrals at large crack extension as shown in the experimental and simulation results. This is a very interesting outcome from this phenomenological cohesive zone modeling approach taken in this investigation. From the viewpoint of the higher J-R curve at large crack extensions of a few mms for the uncharged TS SE(B) specimen when compared with that for the hydrogen-charged TS SE(B) specimen, the higher fracture resistance for the uncharged TS SE(B) specimen is in agreement with the general trend discussed on hydrogen embrittlement in the literature [13, 14].

5. Conclusions

In this investigation, small rectangular single edge bend (SE(B)) specimens were cut from an additively manufactured (AM) 304 stainless steel plate in different orientations and the tensile test specimens were then cut from the fracture tested specimens. Half of the SE(B) specimens before tests were charged with hydrogen. The J-R curves for the uncharged and hydrogen-charged SE(B) specimens of AM stainless steels are first presented. The J-R curves are orientation dependent and the J-R curves for hydrogen-charged SE(B) specimens are lower than those for the uncharged SE(B) specimens. Next, fracture tests of uncharged and hydrogen-charged SE(B) specimens of AM 304 stainless steels are simulated by finite element analyses. The stress-strain relations for the uncharged and hydrogen-charged AM steel specimens of different orientations for use in finite element analyses are fitted from the corresponding tensile

tests of the uncharged AM steels. Two-dimensional plane strain finite element analyses of the uncharged and hydrogen-charged steel SE(B) specimens without cohesive elements are first conducted to determine the values of the cohesive energy for the specimens of the given orientations from the J-integrals of the specimens at crack initiation from the experiments.

Two-dimensional plane strain finite element analyses of the SE(B) specimens with cohesive elements are then conducted. The trapezoidal traction-separation laws are adopted to model the ductile fracture in this investigation. With the initial stiff linear response, the minor influence of the shape factor, and the cohesive energy determined from the experiment, the cohesive strength is the main fitting parameter for each specimen. The computational results indicate that four sets of cohesive parameters can be found to fit the load-displacement-crack extension data and the corresponding J-R curves obtained from the fracture tests of the uncharged and hydrogen-charged steel specimens of different orientations. The simulation results indicated that the phenomenological cohesive zone modeling approach can be used to characterize the crack growths in small SE(B) specimens of AM stainless steels. The best-fit cohesive parameters show that the cohesive strength and energy for the uncharged LS SE(B) specimen are both higher than those for the hydrogen-charged LS SE(B) specimen. The best-fit cohesive parameters also show that the cohesive strength for the uncharged TS SE(B) specimen is higher than that for the hydrogen-charged TS SE(B) specimen while the cohesive energy for the uncharged specimen is lower than that for the hydrogen-charged TS SE(B) specimen.

Acknowledgement

References

[1] Tvergaard, V. and Hutchinson, J.W., The relation between crack growth resistance and fracture process parameters in elastic-plastic solids. Journal of the Mechanics and Physics of Solids. 1992;40:1377–1397. doi:10.1016/0022-5096(92)90020-3.

[2] Tvergaard, V. and Hutchinson, J.W., Effect of T-Stress on mode I crack growth resistance in a ductile solid. International Journal of Solids and Structures. 1994;31:823–833. doi:10.1016/0020-7683(94)90080-9.

[3] Tvergaard, V. and Hutchinson, J.W., Effect of strain-dependent cohesive zone model on predictions of crack growth resistance. International Journal of Solids and Structures. 1996;33:3297–3308. doi:10.1016/0020-7683(95)00261-8.

[4] Roychowdhury, S., Arun Roy, Y.D. and Dodds, R.H., Ductile tearing in thin aluminum panels: experiments and analyses using large-displacement, 3-D surface cohesive elements. Engineering Fracture Mechanics. 2002;69:983–1002. doi:10.1016/S0013-7944(01)00113-8.

[5] Scheider, I. and Brocks, W., Cohesive elements for thin-walled structures. Computational Materials Science. 2006;37:101–109. doi:10.1016/J.COMMATSCI.2005.12.042.

[6] Scheider, I. and Brocks, W., Simulation of cup–cone fracture using the cohesive model. Engineering Fracture Mechanics. 2003;70:1943–1961. doi:10.1016/S0013-7944(03)00133-4.

[7] Cornec, A., Scheider, I. and Schwalbe, K.-H., On the practical application of the cohesive model. Engineering Fracture Mechanics. 2003;70:1963–1987. doi:10.1016/S0013-7944(03)00134-6.

[8] Chen, C.R., Kolednik, O., Heerens, J. and Fischer, F.D., Three-dimensional modeling of ductile crack growth: Cohesive zone parameters and crack tip triaxiality. Engineering Fracture Mechanics. 2005;72:2072–94. doi:10.1016/j.engfracmech.2005.01.008.

[9] Siegmund, T and Brocks, W., A numerical study on the correlation between the work of separation and the dissipation rate in ductile fracture. Engineering Fracture Mechanics. 2000;67:139–154. doi:10.1016/S0013-7944(00)00054-0.

[10] Woelke, P.B., Shields, M.D. and Hutchinson, J.W., Cohesive zone modeling and calibration for mode I tearing of large ductile plates. Engineering Fracture Mechanics. 2015;147:293–305. doi:10.1016/j.engfracmech.2015.03.015.

[11] Griffith, M.L., Ensz, M.T., Puskar, J.D., Robino, C.V., Brooks, J.A., Philliber, J.A., Smugeresky, J.E. and Hofmeister, W.H., Understanding the microstructure and properties of components fabricated by laser engineered net shaping (LENS). MRS Proceedings. 2000;625:9–20. doi:10.1557/PROC-625-9.

[12] Wang, Z., Palmer, T.A. and Beese, A.M., Effect of processing parameters on microstructure and tensile properties of austenitic stainless steel 304L made by directed energy deposition additive manufacturing. Acta Materialia. 2016;110:226–235. doi:10.1016/j.actamat.2016.03.019.

[13] Borchers, C., Michler, T. and Pundt, A., Effect of hydrogen on the mechanical properties of stainless steels. Advanced Engineering Materials. 2008;10:11–23. doi:10.1002/adem.200700252.

[14] Jemblie, L., Olden, V. and Akselsen, O.M., A review of cohesive zone modelling as an approach for numerically assessing hydrogen embrittlement of steel structures. Philosophical Transactions of the Royal Society A: Mathematical, Physical and Engineering Sciences. 2017;375:20160411. doi:10.1098/rsta.2016.0411.

[15] ASTM E1820 Standard Test Method for Measurement of Fracture Toughness, ASTM International, West Conshohocken, PA, 2018. doi:10.1520/E1820-18

[16] Wu, S., Sung, S.-J., Pan, J., Lam, P.-S., Morgan, M. and Korinko, P., Modeling of crack extensions in arc-shaped specimens of austenitic stainless steels without and with charged hydrogen using cohesive zone model. ASME PVP Conference. 2018.

[17] Park, K. and Paulino, G.H., Computational implementation of the PPR potential-based cohesive model in ABAQUS: Educational perspective. Engineering Fracture Mechanics 2012;93:239–262. doi:10.1016/j.engfracmech.2012.02.007.

Appendix A: Stress-Strain Relations for LS and TS SE(B) Specimens

The stress-strain relations for the LS and TS SE(B) specimens are obtained from four tensile tests with the in-plane surfaces of the LS and TS tensile specimens parallel to the LS and TS planes, respectively. The loading directions are in the L and T directions for the LS and TS tensile specimens, respectively. The loading directions of the tensile specimens are consistent with those of the normal directions of the crack planes in the corresponding SE(B) specimens as schematically shown in Figures 1(a) and (b). The LS tensile specimens #28 and #40 were cut from the undamaged part of the LS SE(B) specimen after the fracture test. The TS tensile specimens #16 and #55 were cut from the undamaged part of the TS SE(B) specimen after the fracture test. Figures A1(a) and (b) show the geometric dimensions of LS and TS tensile specimens with vertical gray lines schematically representing the interfaces between layers. Due to the small variation of the cutting processes, these tensile specimens have slightly different dimensions in the width and thickness dimensions. As shown in the figure, the reduced width section has a length of 7.62 mm, a width w, and a thickness t. The dimensions of the width w and thickness t for the four tensile specimens are listed in Table A1. The gauge length in the middle of the reduced width section is 5.08 mm for all tensile specimens. Due to the symmetry conditions, only one eighth of the reduced width section is modeled in each finite element analysis.

Figure A2 shows the finite element model with the nominal size of 0.74 mm by 3.81 mm by 0.62 mm in the X, Y and Z directions for the LS tensile specimen #28. The bottom surface represents the mid-section of the gauge section. The right and left back surfaces represent the symmetry planes, while the right and left front surfaces represent the free surfaces of the gauge section. As marked in Figure A2, the bottom area for the mid-section is reduced to 0.739 mm by

0.62 mm to trigger possible necking in the middle of the LS tensile specimen #28. The smallest element size is 0.05 mm by 0.05 mm by 0.05 mm near the bottom surface of the finite element model or near the middle section of the LS tensile specimen. The three-dimensional quadratic elements with reduced integration (C3D20R) are used. The X, Y and Z symmetry conditions are applied to the left back, bottom and right back surfaces, respectively, and a uniform displacement is applied to the top surface of the finite element model. The finite element model of the LS tensile specimen #40 has the nominal size of 0.745 mm by 3.81 mm by 0.62 mm in the X, Y and Z directions. The bottom area is reduced to 0.744 mm by 0.62 mm to trigger possible necking. Similarly, the finite element models of the TS tensile specimens #16 and #55 have the nominal sizes of 0.74 mm by 3.81 mm by 0.62 mm and 0.735 mm by 3.81 mm by 0.61 mm, respectively, in the X, Y and Z directions. The bottom areas of these models are reduced to 0.739 mm by 0.62 mm and 0.734 mm by 0.61 mm for the TS tensile specimens #16 and #55, respectively. The finite element models for the LS tensile specimen #40, and the TS tensile specimens #16 and #55 are similar to that shown in Figure A2 and will not be shown here.

For the LS tensile specimens #28 and #40, the values of Young's modulus E are determined to be 190 GPa and 166 GPa, respectively. The Poisson's ratio ν of 0.3 is used for both LS tensile specimens. The values of the yield stress σ_0 are determined to be 290 MPa and 291 MPa, respectively. For the TS tensile specimens #16 and #55, the values of Young's modulus E are determined to be 176 GPa and 168 GPa, respectively. The Poisson's ratio ν of 0.3 is used for both TS tensile specimens. The values of the yield stress σ_0 are determined to be 347 MPa and 363 MPa, respectively. For the plastic parts of the stress-strain relations, the initial parts of the true stress-plastic strain curves are determined from the experimental engineering

stress-strain curves before the onsets of the load drops. For the final parts of the true stress-plastic strain curves, a power-law relation is used to extend the initial experimental curves as

$$\sigma = \sigma_0 + k(\varepsilon_p)^n \tag{A1}$$

where σ is the true stress, ε_p is the plastic strain, σ_0 is the yield stress, and k and n are material constants selected to extend the experimental data to large plastic strains. Figures A3(a) and (b) show the experimental true stress-plastic strain curves and the fitted curves for the LS and TS tensile specimens, respectively. The Young's modulus E, the Poisson's ratio v, the yield stress σ_0, and the material constants k and n for the LS and TS tensile specimens are listed in Table A2. It should be mentioned that the initial parts of the true stress-plastic strain curves for the TS tensile specimens are slightly higher than those of the LS tensile specimens. However, the hardening exponents of the fitted true stress-plastic strain curves for the TS tensile specimens are lower than those of the LS tensile specimens. The commercial finite element program ABAQUS was employed to perform the computations with consideration of geometric nonlinearity.

Figures A4(a) and (b) show the engineering stress-strain curves from the experiments and the finite element analyses for the LS and TS tensile specimens. As shown in the figures, the results of the finite element analyses are in agreement with the experimental data before the drops of the experimental curves. The drops occur at the engineering strain of 0.65 and 0.57 for the LS tensile specimens #28 and #40, respectively, and 0.49 and 0.49 for the TS tensile specimens #16 and #55, respectively. At the onsets of the drops, the maximum tensile stresses in the middle of the tensile specimens are about 1,066 MPa and 980 MPa for the LS tensile specimens #28 and #40, respectively, and about 997 MPa and 1,011 MPa for the TS tensile specimens #16 and #55, respectively. Finite element analyses were also conducted with a larger

element size of 0.1 mm by 0.1 mm by 0.1 mm near the bottom of the models. The element size

is comparable to the one used in the finite element models of the SE(B) specimens. The

computational results are consistent to those with the fine meshes.

As shown in Figure A4(a) for the LS tensile specimens, the computational engineering

stress-strain curves reach the maximum and continue with a trend of gradual drop, while the

experiment curves have steep drops at the engineering strains of 0.65 and 0.57 for the two

specimens. As shown in Figure A3(a), the fitted true stress-plastic strain curves in a power-law

form are to extend the initial parts of the curves to larger plastic strains. The possible damage

mechanisms in the LS tensile specimens cannot be modeled by the extensions of the

experimental data. Similarly, the possible damage mechanisms in the TS tensile specimens

cannot be modeled although the fitted curves have less strain hardening so that the large drops

due to necking are shown in the computational results at larger engineering strains in Figure

A4(b).

Table 1. The dimensions for the uncharged and hydrogen-charged LS and TS SE(B) specimens

	LS		TS	
	Uncharged	Hydrogen-charged	Uncharged	Hydrogen-charged
a (mm)	5.939	4.773	5.611	5.669
B (mm)	5.6	5.497	5.532	5.552
B_n (mm)	4.648	4.729	4.63	4.63
W (mm)	10.998	11.148	11.267	11.306
b (mm)	5.059	6.375	5.656	5.637

Table 2. The values of the crack initiation load, the maximum load, the J-integrals at crack initiation and the maximum load, and the crack extensions corresponding to crack initiation and the maximum load for the uncharged and hydrogen-charged LS and TS SE(B) specimens.

	LS		TS	
	Uncharged	Hydrogen-charged	Uncharged	Hydrogen-charged
Crack initiation load F_i (N)	2,050	2,750	2,200	2,400
Maximum load F_{max} (N)	3,030	3,770	3,130	3,000
J-integral at crack initiation, J_i (kJ/m^2)	137	58	40	64
J-integral at maximum load, J_{max} (kJ/m^2)	1,091	618	638	353
Crack extension corresponding to J_i (mm)	0.137	0.144	0.041	0.126
Crack extension corresponding to J_{max} (mm)	0.822	0.915	0.707	0.509

Table 3. Cohesive parameters for the uncharged and hydrogen-charged LS SE(B) specimens.

	Independent parameters			Dependent parameters		
	T_0 (MPa)	Γ_0 (kJ/m²)	δ_2/δ_0	δ_0 (mm)	δ_1 (mm)	δ_2 (mm)
Uncharged	1,600 (5.52 σ_0)	137	0.22	0.1408	0.0007	0.0310
Hydrogen-charged	1,500 (5.17 σ_0)	58	0.3	0.0596	0.0003	0.0179

Table 4. Cohesive parameters for the uncharged and hydrogen-charged TS SE(B) specimens.

	Independent parameters			Dependent parameters		
	T_0 (MPa)	Γ_0 (kJ/m²)	δ_2/δ_0	δ_0 (mm)	δ_1 (mm)	δ_2 (mm)
Uncharged	1,900 (5.48 σ_0)	40	0.3	0.0325	0.0002	0.0097
Hydrogen-charged	1,550 (4.47 σ_0)	64	0.3	0.0637	0.0003	0.0191

Table A1. The dimensions of the width w and thickness t for the LS and TS tensile specimens.

Specimen	Width w (mm)	Thickness t (mm)
LS #28	1.48	1.24
LS #40	1.49	1.24
TS #16	1.48	1.24
TS #55	1.47	1.22

Table A2. The Young's modulus E, the Poisson's ratio ν, the yield stress σ_0, and the material constants k and n for the LS and TS tensile specimens.

Specimen	Young's modulus E (GPa)	Poisson's ratio ν	Yield stress σ_0 (MPa)	k	n
LS #28	190	0.3	290	1248.17	0.7
LS #40	166	0.3	291	1194.07	0.68
TS #16	176	0.3	347	1123.18	0.63
TS #55	168	0.3	363	1128.27	0.63

(a)

(b)

(c)
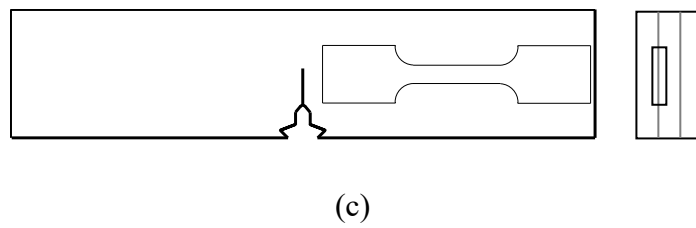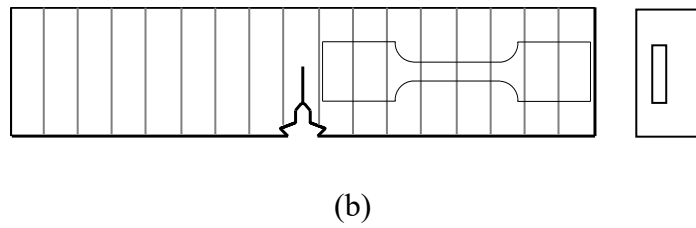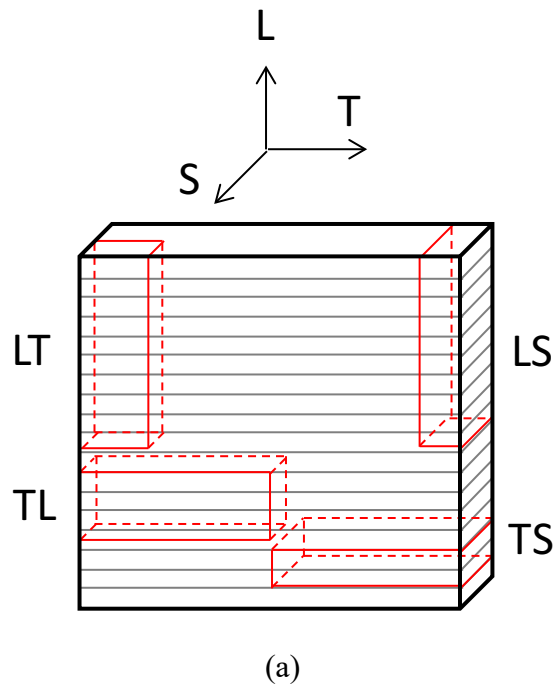
Figure 1. (a) An AM plate, the orientations of the AM plate, and SE(B) specimens of different orientations, schematics of (b) an LS SE(B) specimen, and (c) a TS SE(B) specimen.
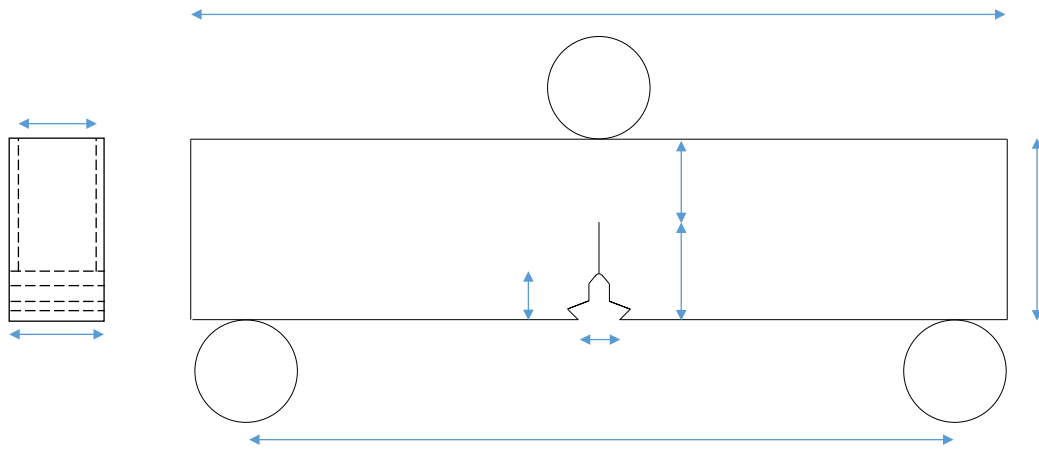
Figure 2. A schematic of an SE(B) specimen with one loading pin and two supporting pins.
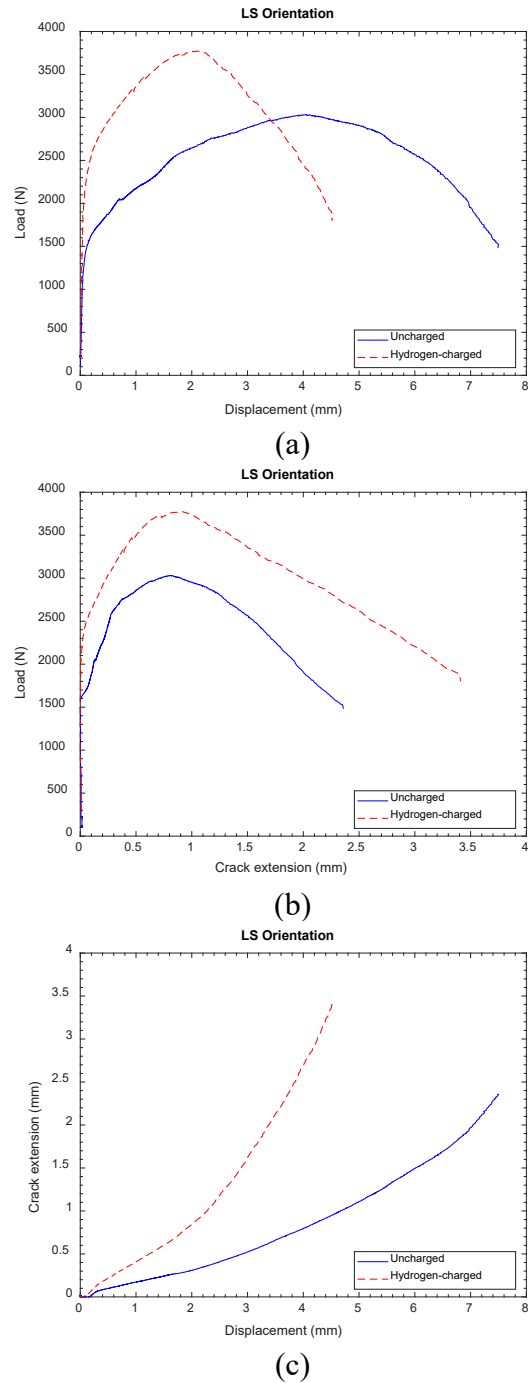
Figure 3. (a) The load-displacement, (b) load-crack extension and (c) crack extension-displacement curves for the uncharged and hydrogen-charged LS SE(B) specimens.

(a)

(b)

(c)
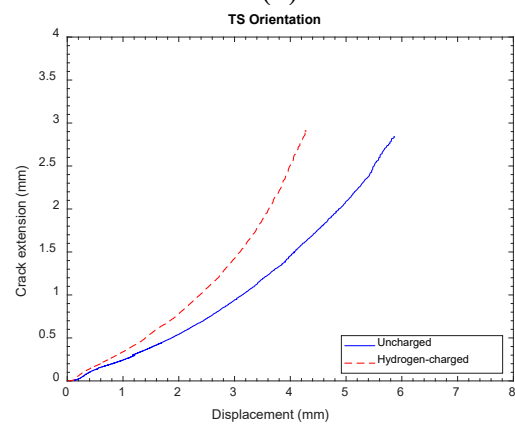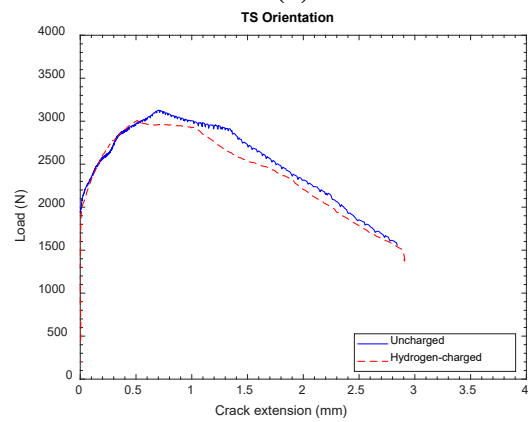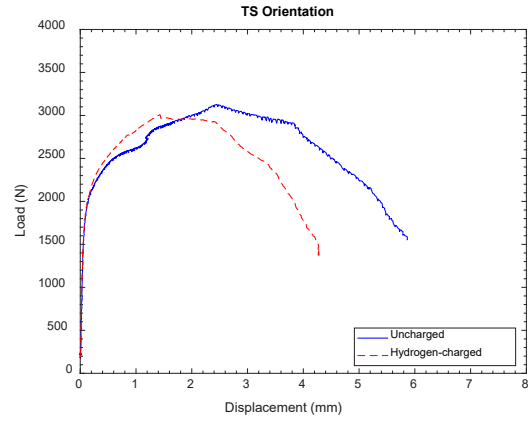
Figure 4. (a) The load-displacement, (b) load-crack extension and (c) crack extension-displacement curves for the uncharged and hydrogen-charged TS SE(B) specimens.
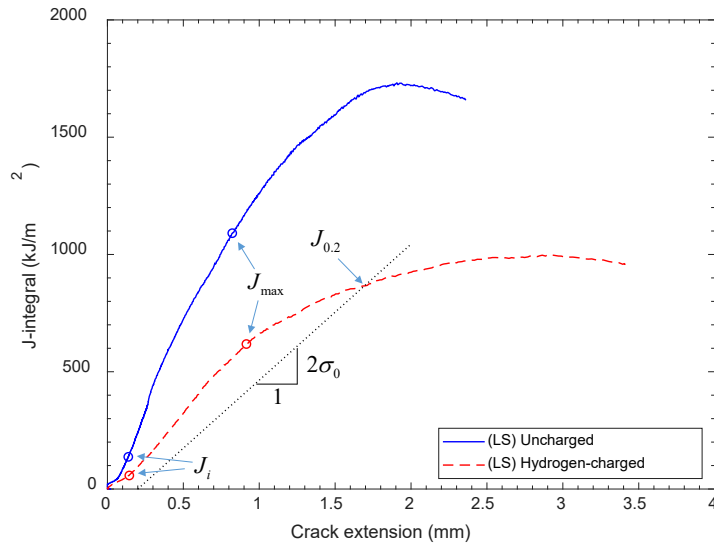
Figure 5. The J-R curves for the uncharged and hydrogen-charged LS SE(B) specimens.
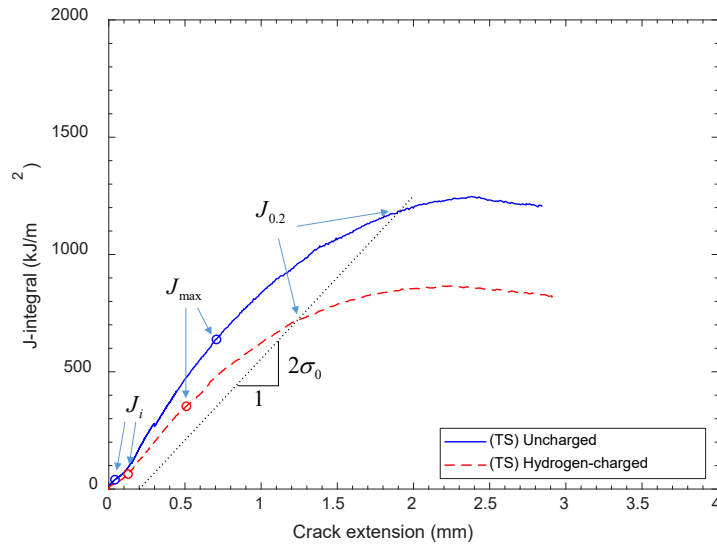
Figure 6. The J-R curves for the uncharged and hydrogen-charged TS SE(B) specimens.
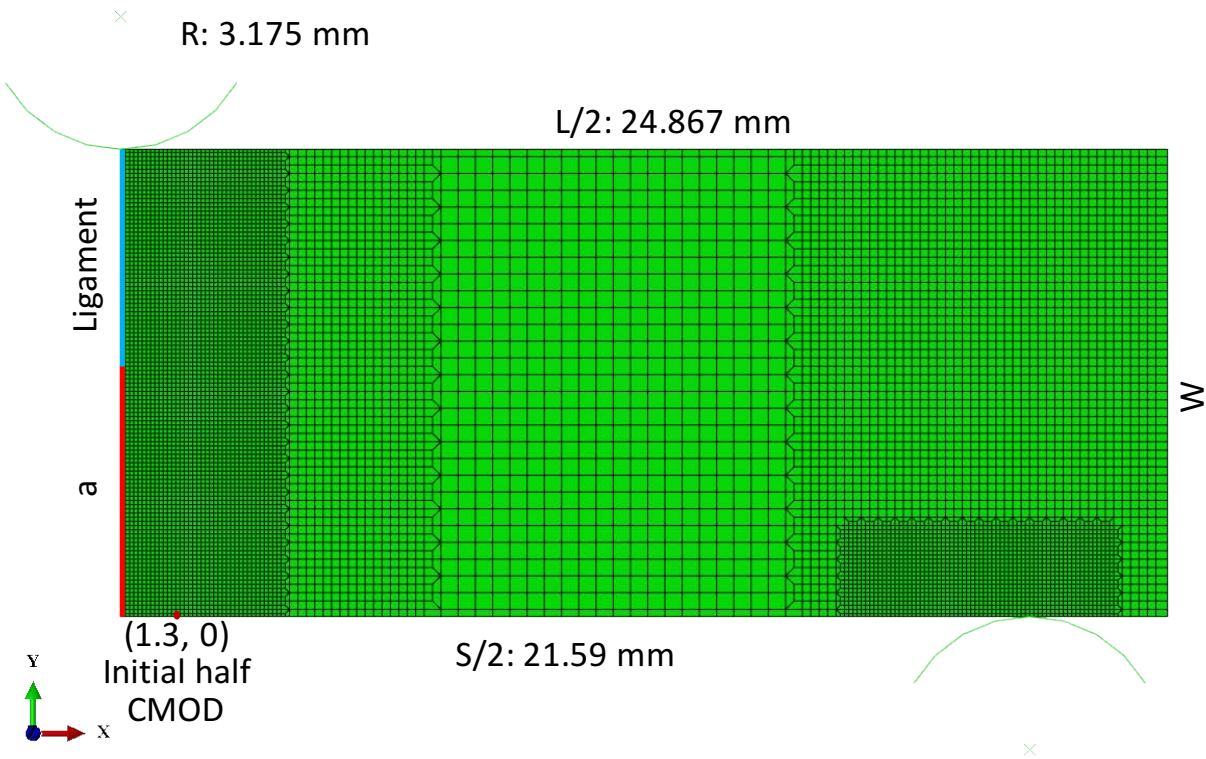
Figure 7. Finite element model of a half of an LS SE(B) specimen.
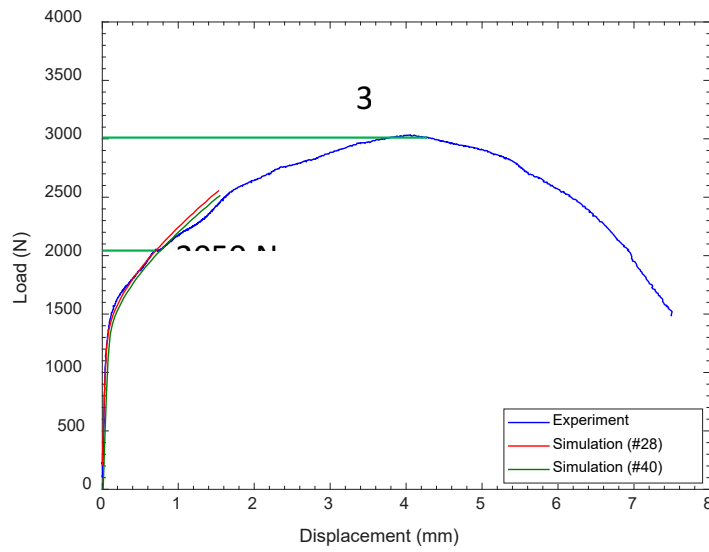
(a)
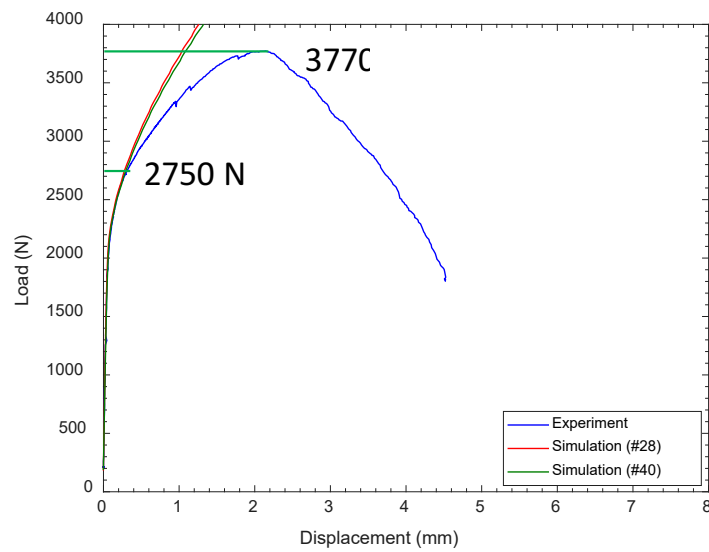
(b)

Figure 8. The computational and experimental load-displacement curves for the (a) uncharged and (b) hydrogen-charged LS SE(B) specimens.
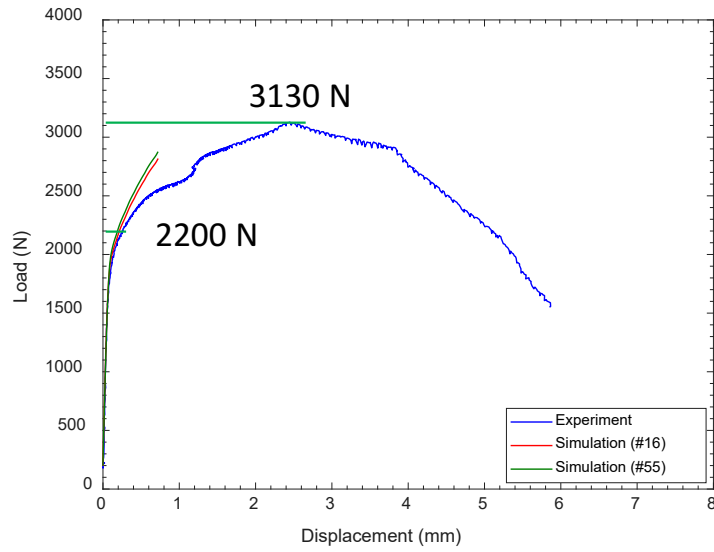
(a)
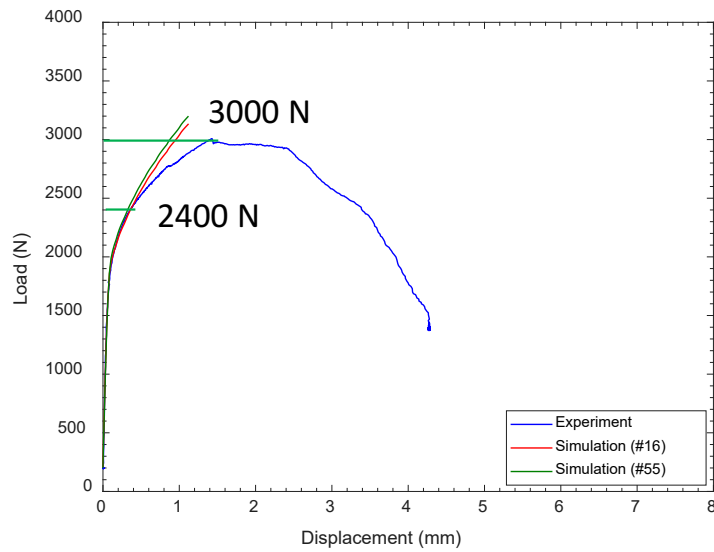
(b)

Figure 9. The computational and experimental load-displacement curves for the (a) uncharged and (b) hydrogen-charged TS SE(B) specimens.
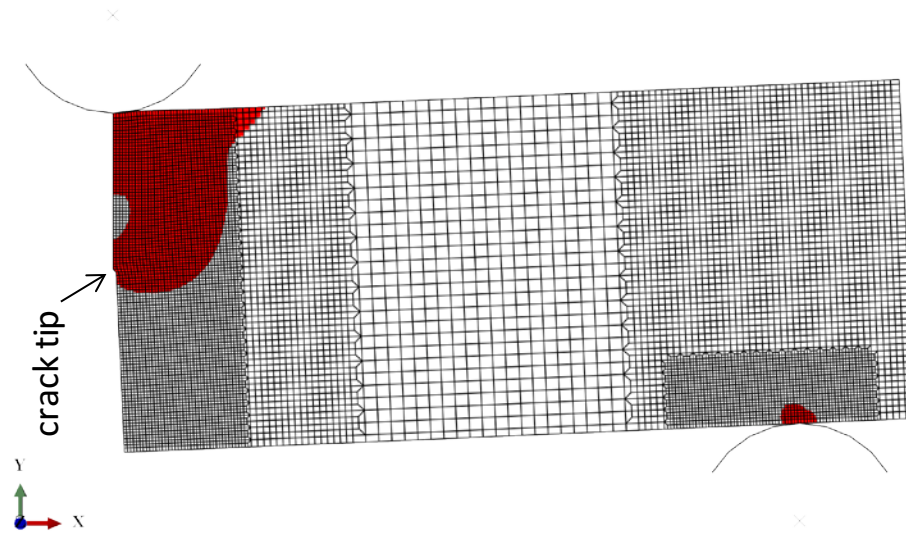
(a)
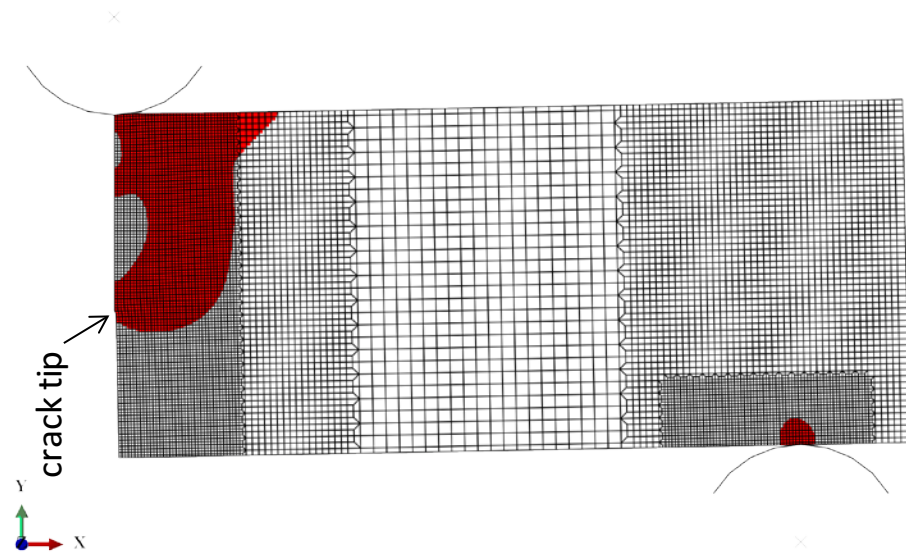
(b)

Figure 10. The plastic zones at crack initiation in the (a) uncharged and (b) hydrogen-charged LS SE(B) specimens.

(a)

(b)
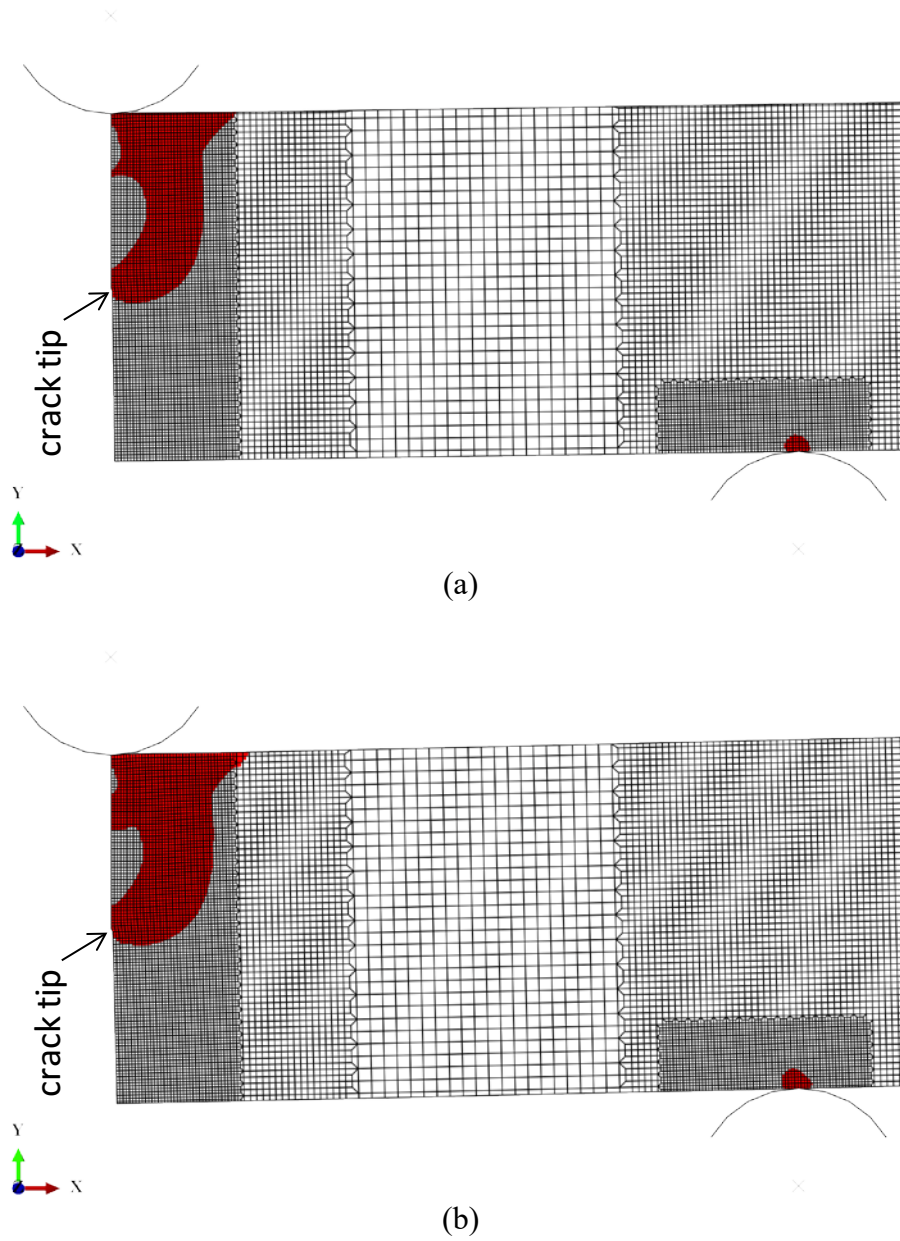
Figure 11. The plastic zones at crack initiation in the (a) uncharged and (b) hydrogen-charged TS SE(B) specimens.
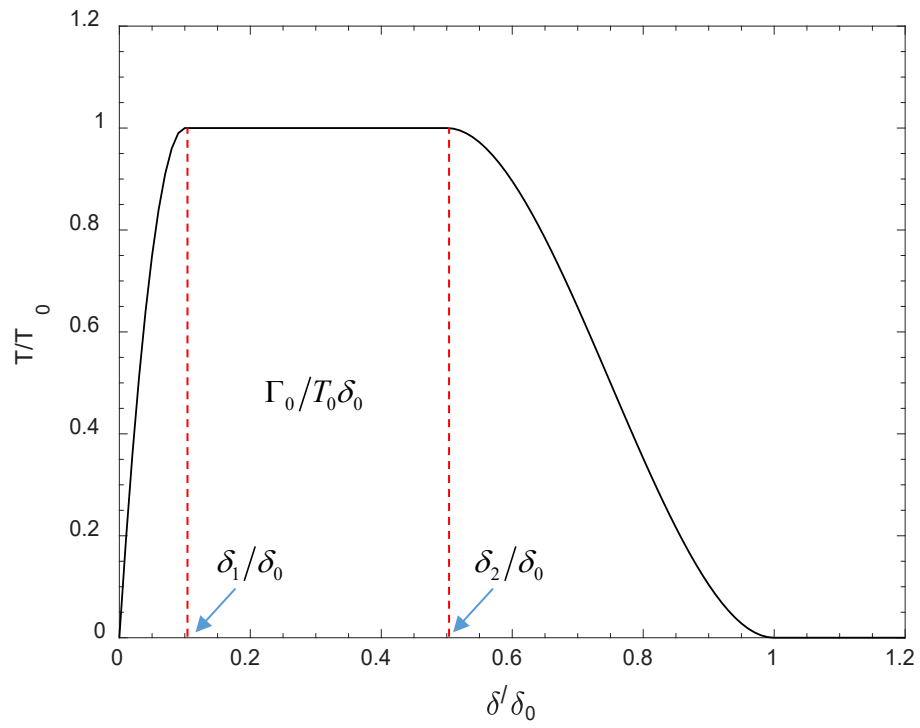
Figure 12. A schematic of a normalized trapezoidal traction-separation law.
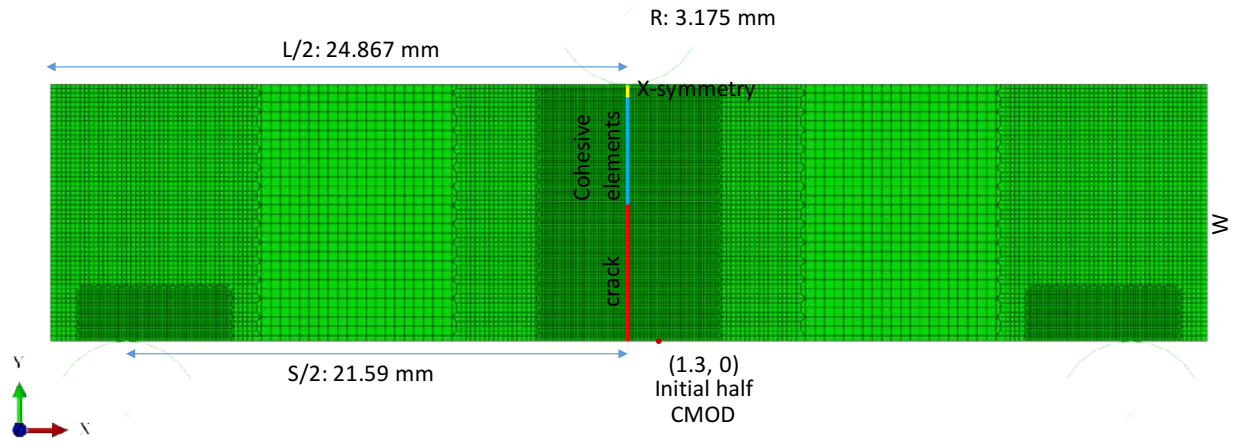
Figure 13. A finite element model of the uncharged LS SE(B) specimen.
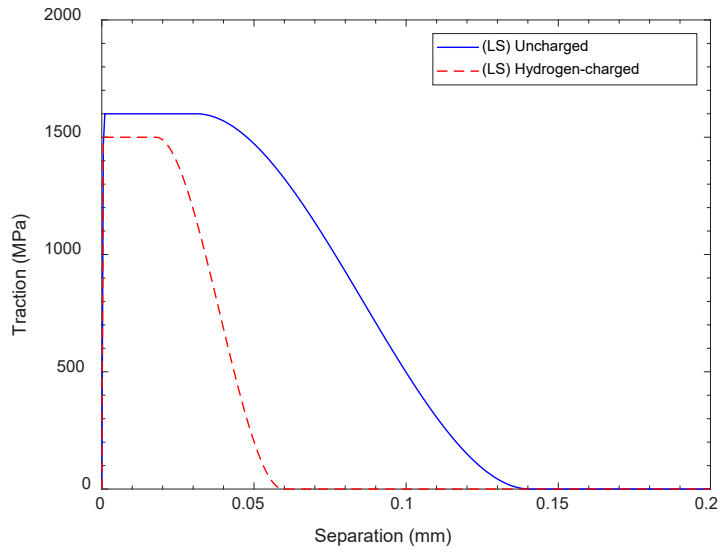
(a)
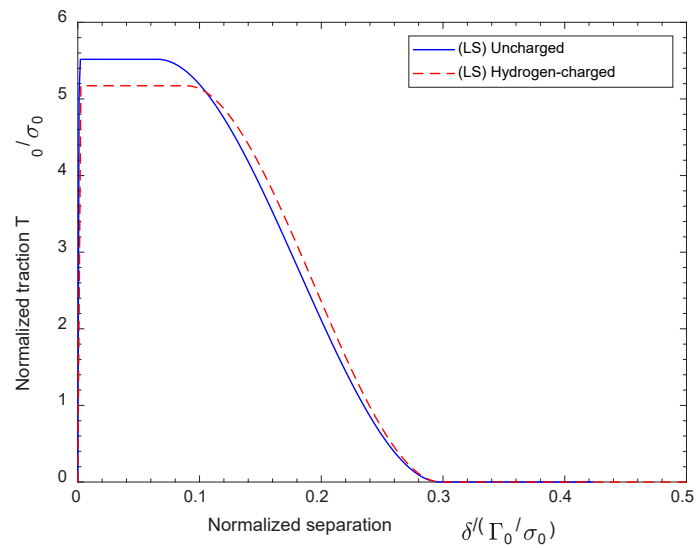
(b)

Figure 14. Schematics of (a) the traction-separation laws and (b) the normalized traction-separation laws for the uncharged and hydrogen-charged LS SE(B) specimens.
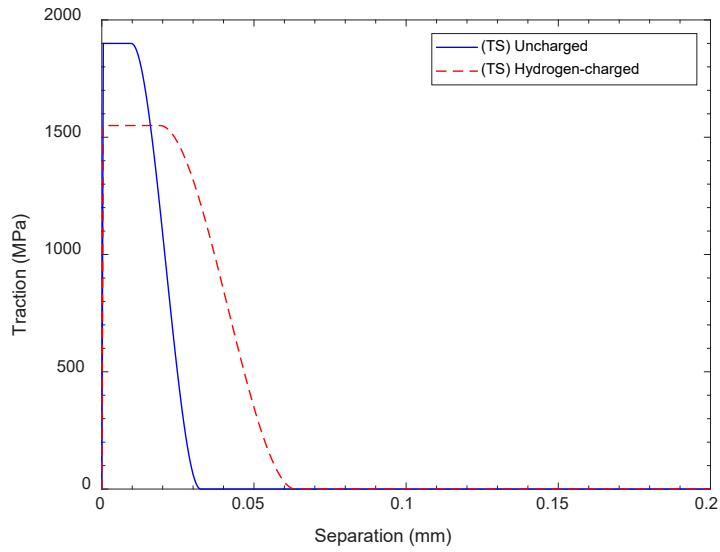
(a)
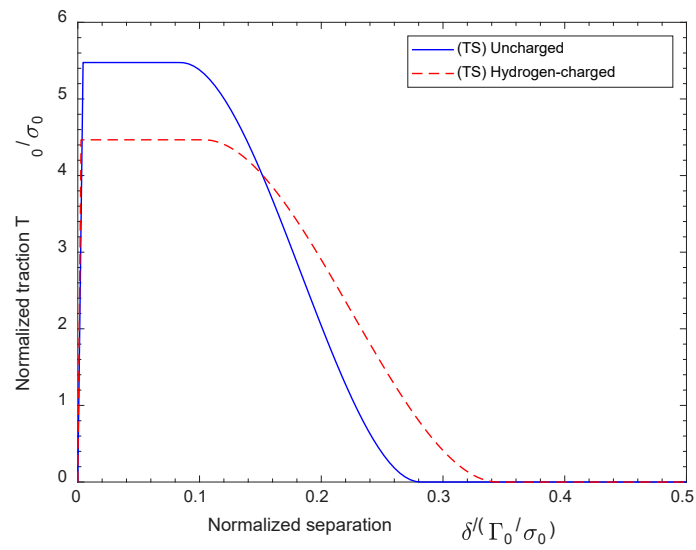
(b)

Figure 15. Schematics of (a) the traction-separation laws and (b) the normalized traction-separation laws for the uncharged and hydrogen-charged TS SE(B) specimens.
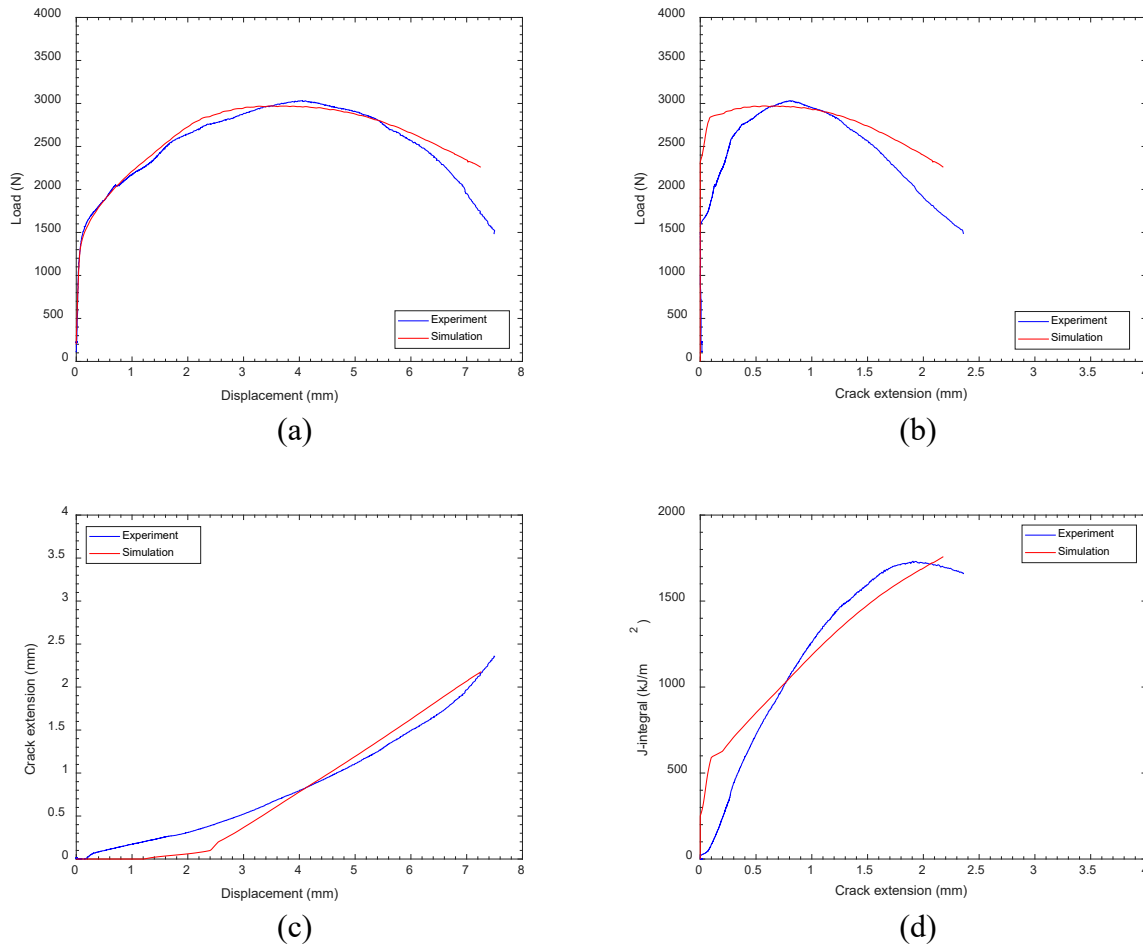
Figure 16. Comparisons of the computational and experimental (a) load-displacement, (b) load-crack extension, (c) crack extension-displacement and (d) J-R curves for the uncharged LS SE(B) specimen.
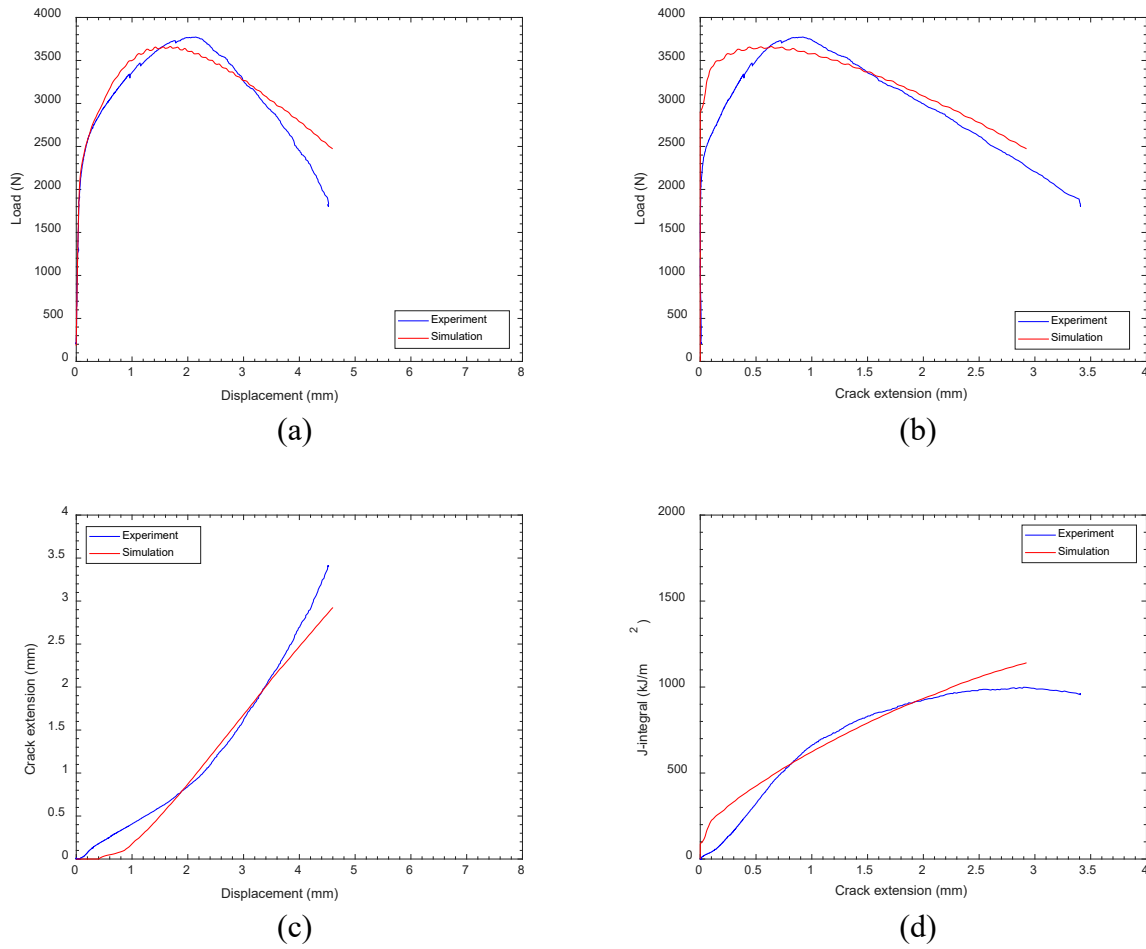
Figure 17. Comparisons of the computational and experimental (a) load-displacement, (b) load-crack extension, (c) crack extension-displacement and (d) J-R curves for the hydrogen-charged LS SE(B) specimen.
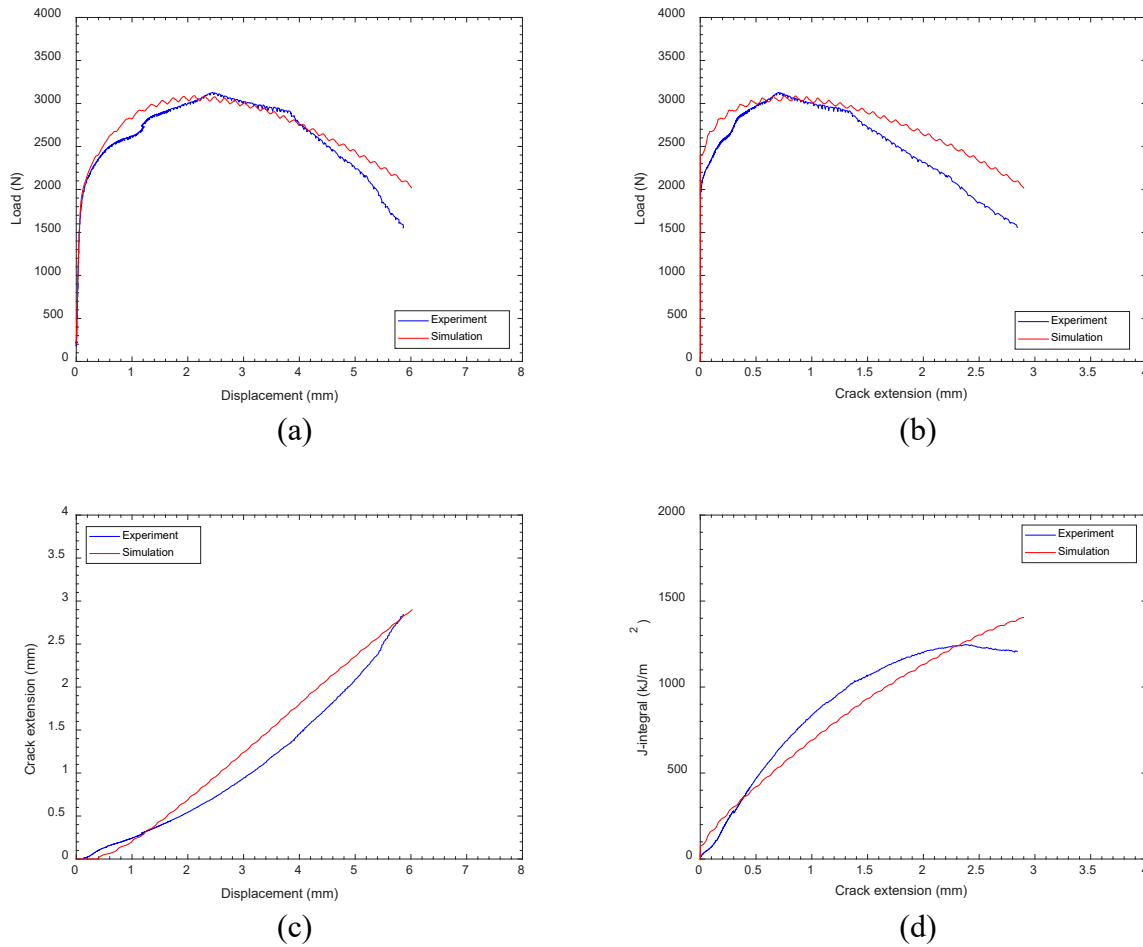
Figure 18. Comparisons of the computational and experimental (a) load-displacement, (b) load-crack extension, (c) crack extension-displacement and (d) J-R curves for the uncharged TS SE(B) specimen.
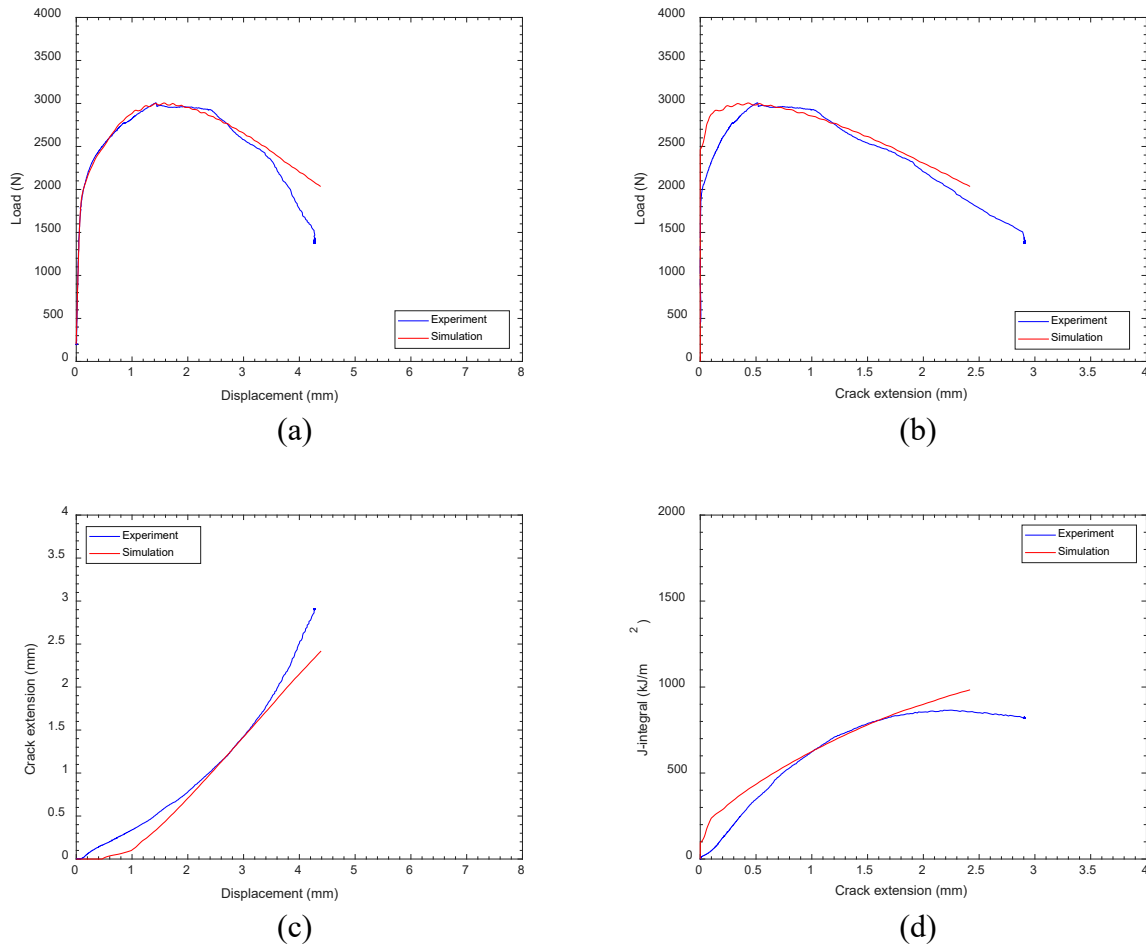
Figure 19. Comparisons of the computational and experimental (a) load-displacement, (b) load-crack extension, (c) crack extension-displacement and (d) J-R curves for the hydrogen-charged TS SE(B) specimen.
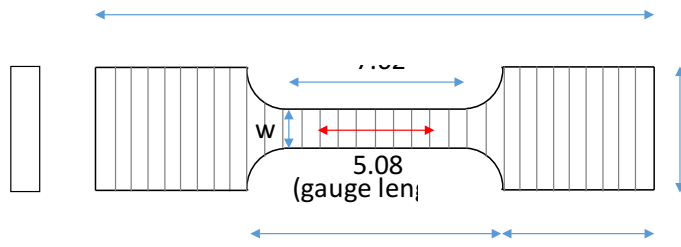
(a)
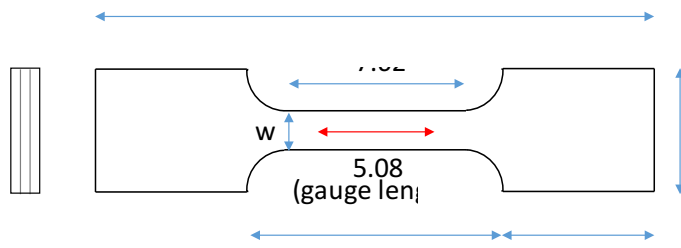
(b)

Figure A1. The geometric dimensions of (a) LS and (b) TS tensile specimens with gray vertical lines schematically representing the interfaces between layers.
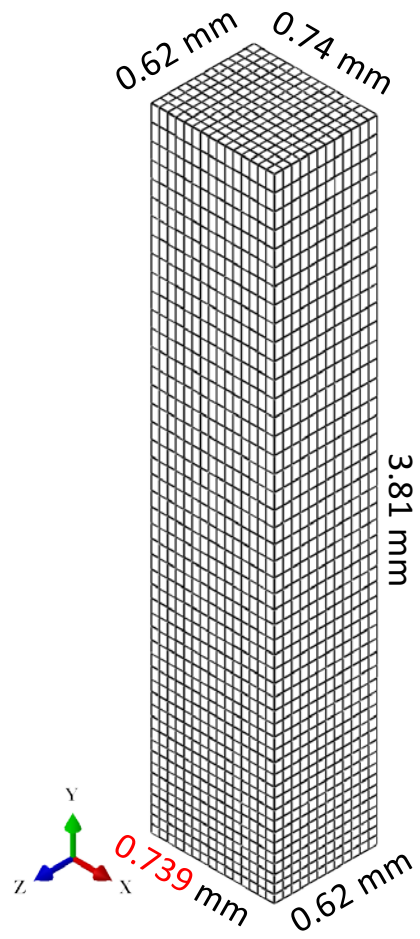
Figure A2. The finite element model of one eighth of the reduced-width section of LS tensile specimen #28.
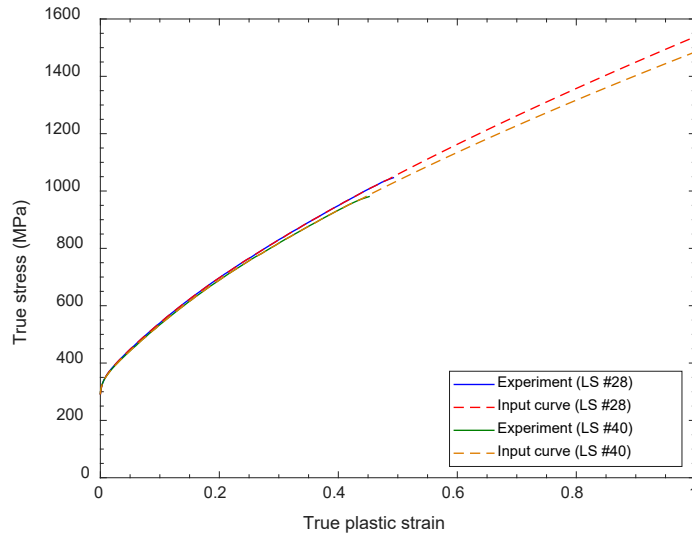
(a)
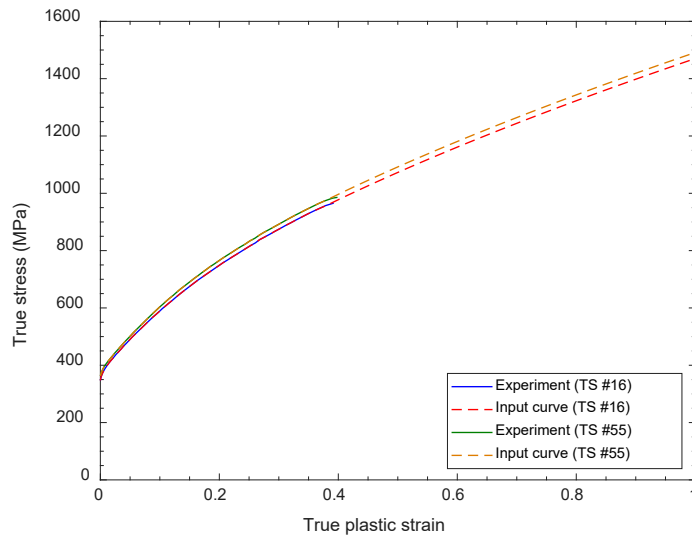
(b)

Figure A3. The experimental and fitted input true stress-true plastic strain curves for (a) LS tensile specimens #28 and #40 and (b) TS tensile specimens #16 and #55.
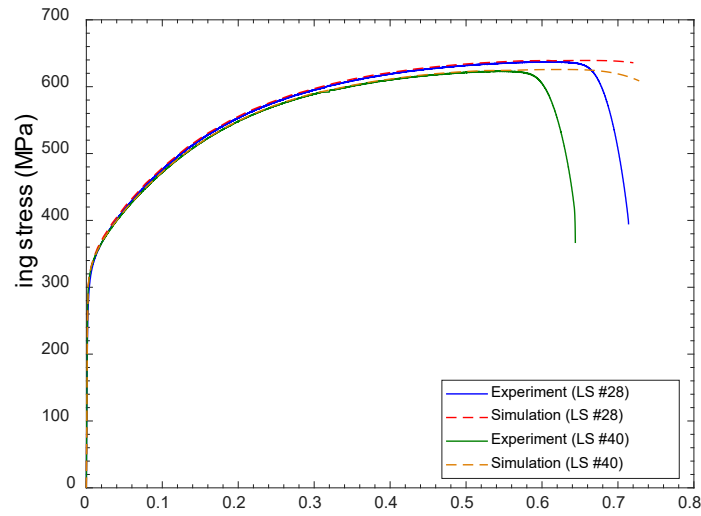
(a)
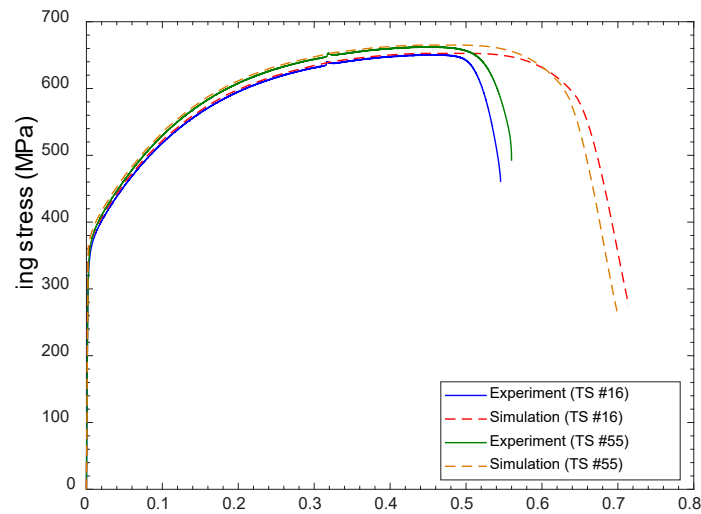
(b)

Figure A4. Comparisons of the engineering stress-strain curves from the experiments and the finite element analyses for (a) LS tensile specimens #28 and #40 and (b) TS tensile specimens #16 and #55.